



RESEARCH ARTICLE

Laser chirp controlled relativistic few-cycle mid-infrared pulse generation

Dongao Li¹, Guobo Zhang², Jie Zhao¹, Yanting Hu¹, Yu Lu¹, Hao Zhang¹, Qianni Li¹,
Dongze Zhang¹, Rong Sha¹, Fuqiu Shao¹, Zhengming Sheng^{3,4,5}, and Tongpu Yu¹

¹Department of Physics, National University of Defense Technology, Changsha, China

²Department of Nuclear Science and Technology, National University of Defense Technology, Changsha, China

³Key Laboratory for Laser Plasmas (MOE) and School of Physics and Astronomy, Shanghai Jiao Tong University, Shanghai, China

⁴Collaborative Innovation Center of IFSA, Shanghai Jiao Tong University, Shanghai, China

⁵Tsung-Dao Lee Institute, Shanghai Jiao Tong University, Shanghai, China

(Received 29 January 2023; revised 1 May 2023; accepted 12 June 2023)

Abstract

Relativistic few-cycle mid-infrared (mid-IR) pulses are unique tools for strong-field physics and ultrafast science, but are difficult to generate with traditional nonlinear optical methods. Here, we propose a scheme to generate such pulses with high efficiency via plasma-based frequency modulation with a negatively chirped laser pulse (NCLP). The NCLP is rapidly compressed longitudinally due to dispersion and plasma etching, and its central frequency is downshifted via photon deceleration due to the enhanced laser intensity and plasma density modulations. Simulation results show that few-cycle mid-IR pulses with the maximum center wavelength of 7.9 μm and pulse intensity of $a_{\text{MIR}} = 2.9$ can be generated under a proper chirp parameter. Further, the maximum energy conversion efficiency can approach 5.0%. Such a relativistic mid-IR source is promising for a wide range of applications.

Keywords: chirp laser pulses; laser wakefield; photon deceleration; relativistic mid-infrared generation

1. Introduction

Over the past few decades, laser pulses have been widely used in fundamental science, industry, medicine and so on. In particular, the laser–matter interaction has entered into the relativistic regime due to the invention of the chirped pulse amplification (CPA) technique^[1]. Currently, the theoretical and experimental studies in this regime have mainly used Ti:sapphire and Nd:glass laser pulses with wavelengths of 0.8 or 1.0 μm ^[2–6]. However, pulses in other wavelength bands, such as mid-infrared (mid-IR), are attracting increasing interest due to many applications, such as 2D infrared spectroscopy^[7] and time-resolved imaging of molecular structures^[8]. On the other hand, when the mid-IR pulse is enhanced to relativistic intensity,

it can also be widely used in the laser interaction with matter, such as in the detection of electron energy^[9], terahertz (THz) emission^[10], high-order harmonic generation (HHG)^[11,12] and charged particle acceleration^[13–15], all of which would benefit from the long carrier wavelength, few-cycle duration and high peak intensity of the mid-IR pulse. To date, high-intensity mid-IR pulses have been achieved via traditional nonlinear optical methods, for example, optical parametric amplification^[16,17], difference frequency generation^[18,19], four-wave mixing^[20] and optical rectification^[21,22]. Moreover, the CO₂ laser obtained in a gas medium is also an important source of the high-intensity mid-IR pulse^[23,24]. However, due to the damage threshold of the optical crystal, it is still challenging to generate mid-IR pulses with relativistic intensity, few cycles and controllable carrier wavelengths. In recent years, plasma-based optical modulation has received significant attention, and several effective schemes have been proposed to obtain high-intensity mid-IR pulses, such as the plasma optical modulator^[25], synchrotron

Correspondence to: Guobo Zhang, Department of Nuclear Science and Technology, National University of Defense Technology, Changsha 410073, China. Email: zgb830@163.com; Tongpu Yu, Department of Physics, National University of Defense Technology, Changsha 410073, China. Email: tongpu@nudt.edu.cn

by the NCLP, that is, the high-frequency component first and low-frequency second, can be divided into three stages: (I) the wakefield excitation stage; (II) the electron layer compression stage; and (III) the pulse converter stage. In stage (I), the NCLP excites a bubble to move forward at the group velocity of the drive laser pulse. At the same time, each frequency component of the NCLP produces a special curving profile of the refractive index, as shown by the green curve, and the photons in the range of $\partial\eta/\partial\xi < 0$ move backward and others in the range of $\partial\eta/\partial\xi > 0$ move forward, as directed by the blue arrows, which together with the plasma etching lead to the rapid compression of the NCLP in the longitudinal direction. Finally, the pulse width becomes shorter and the laser peak intensity increases dramatically after propagation of a few Rayleigh lengths at stage (II), so that the compressed pulse enters the mid-IR converter stage. At this point, stage (III), the photons are rapidly decelerated due to the greater negative refractive index gradient, and then the generated mid-IR pulse slips backward into the bubble and propagates forward together with the bubble.

Photon deceleration is caused essentially by plasma optical modulation. The basic physics of mid-IR generation in plasma by the NCLP can be interpreted by 1D nonlinear theory^[29]. The electric field of a CLP with the polarization along the y -direction that propagates along the x -direction can be expressed as follows:

$$E_L(t) = E_{L0} \exp\left(-\frac{r^2}{w_0^2}\right) \sin^2\left(\frac{\pi t}{\tau_d}\right) \sin[\omega(t)t], \quad (1)$$

where E_{L0} is the initial peak electric field, w_0 is the spot size and τ_d is the full length of the laser pulse. Here, $\omega(t) = \omega_0[1 - b(t/T_0 - t_c/T_0)]$ is the local longitudinal frequency of a linearly CLP, where $\omega_0 = 2\pi c/\lambda_0$ is the center angular frequency, λ_0 is the center wavelength of the CLP, c is the speed of light in a vacuum, T_0 is the laser period, $t_c = \tau_d/2$ is the initial center of the laser pulse and b is the linear chirp parameter. Here, we assume $b > 0$ for a PCLP and $b < 0$ for an NCLP.

The interaction of relativistic CLPs with underdense plasma can be described by the coupled equations under the Coulomb gauge^[40,41,48–51]:

$$\left(2c \frac{\partial^2 a}{\partial \xi \partial \tau} - \frac{\partial^2 a}{\partial \tau^2}\right) = c^2 k_p^2 \frac{a}{1 + \phi}, \quad (2)$$

$$2 \frac{\partial^2 \phi}{\partial \xi^2} = k_p^2 \left[\frac{1 + p_y^2}{(1 + \phi)^2} - 1 \right], \quad (3)$$

where $a(\xi) = [eA(\xi)]/(m_e c^2)$ and $\phi(\xi) = [e\Phi(\xi)]/(m_e c^2)$ are the normalized vector and scalar potentials associated with the laser pulse and the wakefield, respectively. Here,

$\xi = x - ct$ and $\tau = t$ are in the laser-rest frame, $k_p = \omega_p/c$ is the plasma wave number, $\omega_p = \sqrt{(4\pi n_e e^2)/m_e}$ is the plasma frequency, c is the speed of light in a vacuum, e is the unit charge, n_e is the plasma density and m_e is the electron mass. Equation (3) can be solved numerically by the fourth-order Runge–Kutta method. In Equation (3), $p_y = p_{y0} + A$ is the transverse momentum component of electrons and A is defined as $A \sim \int_{\xi_0}^{\xi} E_L(\xi') d\xi'$, where $\xi_0 = \xi(\tau = 0)$ and p_{y0} are the initial position and momentum of the plasma electron, respectively. Considering a cold plasma, $p_{y0} = 0$, the transverse momentum completely depends on the laser pulse. Compared with the un-chirped laser pulse, electrons driven by a CLP can still have a nonzero transverse momentum, which is constant behind the pulse.

From Equation (2), we can get the refractive index of a CLP as follows:

$$\eta(\tau) \simeq 1 - \frac{\omega_p^2}{2\omega^2(\tau)} \frac{1}{1 + \phi}, \quad 0 < \tau < \tau_d. \quad (4)$$

Therefore, the phase velocity and the group velocity can be expressed as $v_p(\tau) \simeq c \left\{ 1 + \left[\omega_p^2/2\omega^2(\tau) \right] [1/(1 + \phi)] \right\}$ and $v_g(\tau) \simeq c \left\{ 1 - \left[\omega_p^2/2\omega^2(\tau) \right] [1/(1 + \phi)] \right\}$, respectively. Here, ϕ is the solution of Equation (3).

The wavelength changes of the drive laser in a short time duration $\Delta\tau$ can be estimated by $\lambda = \lambda_0 + \lambda_0 \Delta\tau \partial v_p/\partial \xi$ ^[37], and $\lambda_0 \partial v_p/\partial \xi$ is the difference of the phase velocity between the two adjacent crests. Then, using $v_p = c\eta^{-1}$, the change of λ gives the following:

$$\lambda = \lambda_0 \left(1 - c \int_0^{t_i} \eta^{-2} \frac{\partial \eta}{\partial \xi} d\tau \right), \quad (5)$$

where t_i is the interaction time, $\partial\eta/\partial\xi > 0$ implies photon acceleration and $\partial\eta/\partial\xi < 0$ means photon deceleration.

We assume an average refractive index gradient of $-\partial\eta/\partial\xi \sim 3 \times 10^{-3} \mu\text{m}^{-1}$ for the case presented here when $a_0 > 1$, and thus the wavelength modulation can be estimated by Equation (5), which is as high as $10\lambda_0$ over an interaction distance of about 3 mm. Due to the longitudinal compression of the NCLP, the drive pulse can excite a larger negative refractive index gradient.

3. Relativistic mid-infrared pulse generation

For the quantitative description for the generation of mid-IR pulses by NCLP interaction with underdense plasma, we first perform a series of 2D particle-in-cell (PIC) simulations by using the open source PIC code EPOCH^[52]. The normalized vector potential of the laser pulse is $a_0 = 2$, the peak intensity is $I_0 = 8.6 \times 10^{18} \text{ W cm}^{-2}$ and the center wavelength of the CLPs is $\lambda_0 = 0.8 \mu\text{m}$, while $w_0 = 15 \mu\text{m}$ and

$\tau_d = 20T_0$ are the spot size and pulse duration, respectively, where $T_0 \approx 2.64$ fs is the laser period. The effective chirp parameter range of the CLP, that is, $-0.1 < b < 0.1$, can be obtained by considering $1 - b(t/T_0 - t_c/T_0) > 0$ when $0 < t < 20T_0$ and $t_c = 10T_0$. The incident laser pulse has a spatial-temporal profile as defined by Equation (1) with the chirp parameter $b = -0.07$, which corresponds to a pulse energy of about 803 mJ, a full width at half maximum (FWHM) of the spectrum of about 500 nm and a chirp rate of $R = W/T \approx 18.9$ nm/fs^[53]. Here, W is the FWHM of the spectrum and T is the FWHM of the pulse duration. Such a bandwidth pulse may be achieved by induced-phase modulation (IPM)^[54] with fused silica plates. A plasma channel is used to guide the propagation of focused laser pulses over many Rayleigh lengths^[55] and to excite a stable bubble structure. The simulation box has a total longitudinal length of 3500 μm , and the moving window technology is used. The size of the moving window is 80 μm (x) \times 70 μm (y) with grid cells of 2400×1400 and 16 macroparticles per cell. The parabolic plasma channel has the transverse density distribution of $n_e = n_0 + \Delta n r^2/w_0^2$ with a 100 μm up ramp, a 3200 μm plateau and a 50 μm down ramp, where $n_0 = 3 \times 10^{18} \text{ cm}^{-3}$ is the background electron density on-axis, $\Delta n = n(w_0) - n(0) = 1.13 \times 10^{20}/w_0^2$ (μm) is the channel depth with the matched laser spot size^[55] and r is the radial distance from the channel axis. This plasma channel can be generated in several ways, which have been widely used in laser-plasma experiments^[55–57].

Figures 2(a)–2(c) show the evolution of the transverse electric field (E_y) of the drive laser and the electron density distribution (n_e), together with longitudinal electron density on-axis. In stage (I), one can see from Figure 2(a) that a stable bubble can be excited, and the laser pulse is located in front of the bubble. The length of the bubble corresponds to the plasma wavelength $\lambda_p = (2\pi c)/\sqrt{(4\pi n_e e^2)/m_e} = 19.3 \mu\text{m}$, and the maximum density perturbation is only $6 \times 10^{18} \text{ cm}^{-3}$. Here, the density up ramp of stage (I) can guide the NCLP propagation into the plasma without causing boundary electron injection, and it has almost no effect on the frequency profile of the laser pulses. After that, in stage (II) of Figure 1, the FWHM of the NCLP rapidly compresses to 9 fs when the propagation distance is 1.8 mm, which is well below the initial pulse width, as shown in Figure 2(b). Meanwhile, a small frequency downshift (about 2 μm) can be seen, represented by the black curve in Figure 2(e). With the compression of the drive laser in stage (II), the peak electric field of the NCLP can approach $1.7 \times 10^{13} \text{ V m}^{-1}$, and the plasma density in front of the bubble is increased in excess of $3 \times 10^{19} \text{ cm}^{-3}$ at $t = 2250T_0$. The enhanced density peak provides a large negative refractive index gradient $\partial\eta/\partial\xi$, as shown in Figure 1, leading to more efficient photon deceleration. For example, at $t = 2250T_0$, one can estimate $\partial\eta/\partial\xi \approx -8 \times 10^{-3} \mu\text{m}^{-1}$. Therefore, compared with the unchirped pulse, the NCLP can rapidly obtain a large refractive index gradient in a shorter plasma by severe compression. After $t = 2250T_0$, the pulse enters into stage (III), where

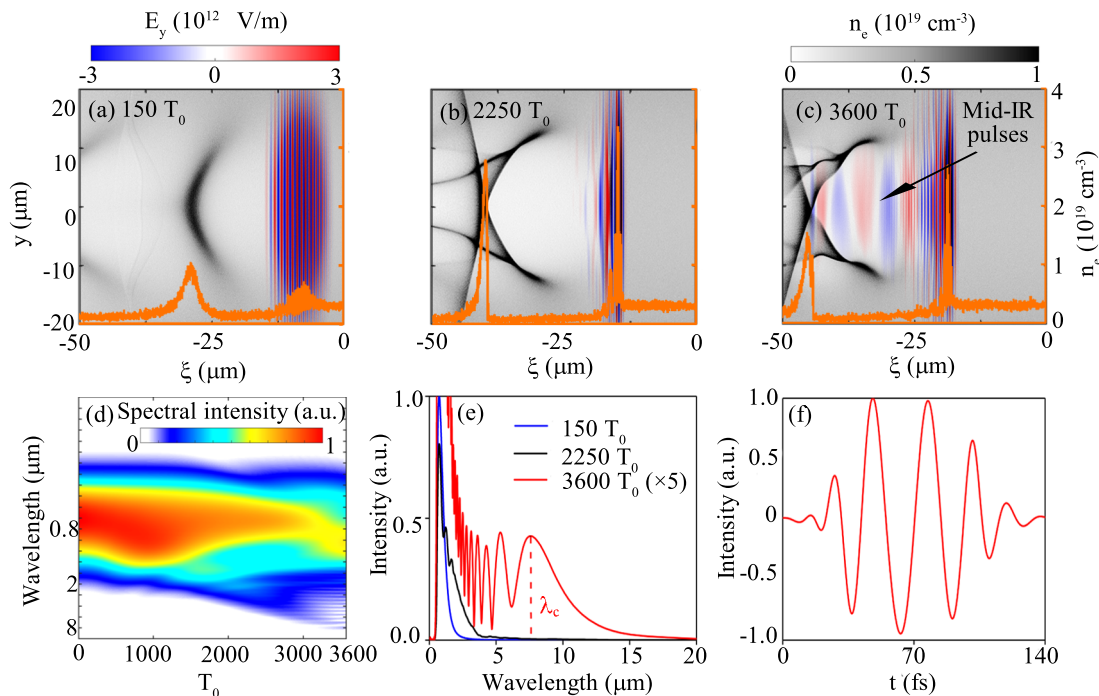


Figure 2. 2D simulation of mid-IR generation with the NCLP. (a)–(c) Distributions of the plasma density (n_e) and transverse electric field (E_y) at different times. The orange curve is the electron density on-axis. (d) Spectral evolution as a function of the propagation time. (e) Spectral distribution of the on-axis laser electric field at $t = 150T_0$ (blue), $2250T_0$ (black) and $3600T_0$ (red). (f) Temporal profile of the mid-IR electric field at $t = 3600T_0$.

the large refractive index gradient leads to a rapid frequency downshift of photons. Assuming the number of photons to be constant, that is, regardless of the energy loss, the frequency downshift of photons will lead to a reduction of the laser pulse energy, which manifests as deceleration. Therefore, the low-frequency mid-IR pulse slips backward, and fills the entire bubble, as shown in Figure 2(c). The on-axis spectral evolution is shown in Figure 2(d), where one can see that the laser experiences a red-shift steadily before the pulse is compressed. Then the photons constantly slow down. As a result, the spectrum shows multiple mid-IR components. Figure 2(e) shows the spectral distributions at different times. A mid-IR pulse is generated with the maximum center wavelength of $\lambda_c = 7.9 \mu\text{m}$ at $t = 3600T_0$. Figure 2(f) shows the temporal profile of the mid-IR pulse at $t = 3600T_0$. The temporal FWHM of the mid-IR pulse is approximately 56.8 fs and the number of optical cycles is roughly 2.2. Considering the peak electric field of mid-IR pulses with $E_{\text{MIR}} \approx 1.1 \times 10^{12} \text{ V m}^{-1}$, the normalized pulse intensity can be estimated as $a_{\text{MIR}} = (e\lambda_c E_{\text{MIR}}) / (2\pi m_e c^2) \approx 2.9$. Therefore, it is a relativistic, few-cycle and long-wavelength mid-IR pulse.

The compression of the NCLP enhances the generation efficiency of the mid-IR pulse and shortens the length of the plasma. Therefore, in order to investigate the pulse compression process in detail, we present the refractive index distribution of the drive laser. Figure 3 shows the

refractive index and the evolution of pulse length of the NCLP. Meanwhile, the case without chirp is also given for comparison. Since both the v_p and v_g are a function of laser frequency, the NCLP has different distribution of refractive index η , SPM and GVD for different frequency component. Figures 3(a) and 3(b) show the laser electric field and refractive index at $t = 150T_0$ for the cases of the chirp parameter $b = -0.07$ and un-chirped laser pulses, respectively, where the results marked by the red curve (η_{PIC}) come from the PIC simulation, and those marked by the black curve (η_t) are the analytical results from Equation (4). For the NCLP, due to the change of frequency component, we have $\partial\eta/\partial\xi > 0$ caused by the fall of the refractive index at the low-frequency part of the NCLP, where the fall edge is experiencing a photon acceleration. However, for the un-chirped pulse, the refractive index is close to that at the tail of pulse.

To record the distance between the reference points and the pulse center, the position change of the rise edge and the fall edge in the propagation process is shown in Figures 3(c) and 3(d). Due to the plasma etching in the wakefield, the rise edges of the NCLP and un-chirped pulse both compress toward the center of the pulse, as shown by the red dots in Figures 3(c) and 3(d). However, the fall edge of the NCLP also compresses toward the center due to the positive refractive index gradient (photon acceleration). Therefore, at the earlier stage of interaction, the longitudinal

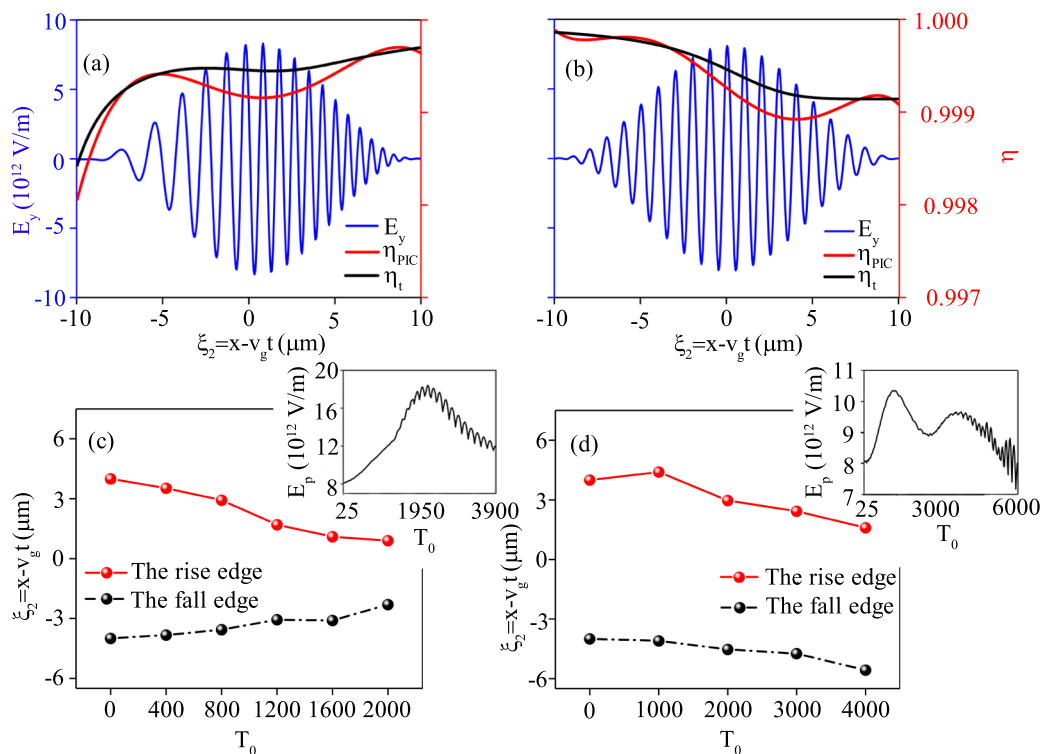


Figure 3. Comparison of refractive index and evolution of the NCLP and un-chirped pulse. Longitudinal distribution of the laser electric field and refractive index in the cases of (a) $b = -0.07$ and (b) an un-chirped laser. (c), (d) The corresponding locations of the rise edge and the fall edge, corresponding to the case with and without chirp, respectively. The insets of (c) and (d) show the evolution of the laser peak electric field E_p .

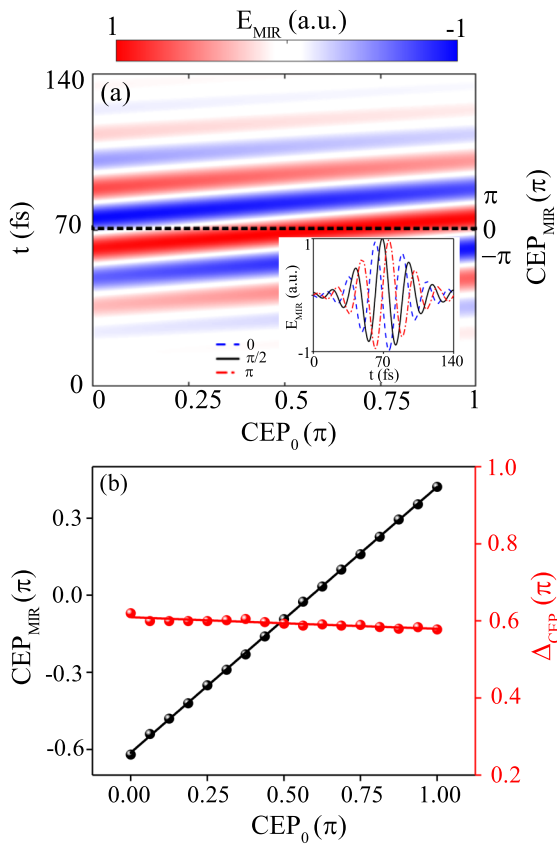


Figure 4. The evolution of the CEP at $t = 3600T_0$. (a) The generated mid-IR electric field as a function of the initial drive pulse phase CEP_0 . The inset shows the electric field waveform for different CEP_0 of the initial drive pulse (0, blue dashed; $\pi/2$, black solid; π , red dot dash). (b) The phase evolution of the mid-IR electric field with CEP_0 variation.

bunching effect of the NCLP results from the photon acceleration and plasma etching. This compression on both edges results in a dramatic increase in pulse intensity and the efficient generation of a mid-IR pulse. The insets of Figures 3(c) and 3(d) show the evolution of the peak laser electric field. One can see that the intensity of the NCLP is significantly enhanced, approaching its maximum value of about $1.8 \times 10^{13} \text{ V m}^{-1}$ ($9.2 \times 10^{12} \text{ V m}^{-1}$ for the case of the un-chirped laser) at $t = 2000T_0$, which verifies the feasibility of the chirped pulse compression scheme in Figure 1. After that, the electric field intensity gradually decreases due to the generation of mid-IR frequency components and the defocusing effect of the drive laser.

The generated mid-IR pulse by photon deceleration is a few-cycle pulse, and its CEP is very important for subsequent applications, since the CEP can directly affect the process of laser-matter interaction. Due to the difference between the phase velocity and the group velocity of waves of different frequency, there must be a phase slip between the drive NCLP CEP_0 and the generated mid-IR pulse CEP_{MIR} . When the CEP is dephased by 2π , the propagation length of pulse is $L_{2\pi} \simeq (n_c/n_e)\lambda_0$ [58]. Therefore, the CEP shift of the NCLP can be expressed as follows:

$$\begin{aligned} \Delta_{CEP} &= CEP_0 - CEP_{MIR} \\ &\approx 2\pi \times \left(\frac{n_e l}{n_c \lambda_0} - \lfloor \frac{n_e l}{n_c \lambda_0} \rfloor \right), \end{aligned} \quad (6)$$

where $\lfloor \rfloor$ is the least integer function and l is the length of the mid-IR pulse generation time. The phase of the generated mid-IR pulse should be consistent with that of the drive laser at the mid-IR pulse generation time. Then, the mid-IR pulse slips rapidly backwards into the bubble, where there are almost no electrons, that is, $\omega_p \approx 0$, $v_p \approx v_g \approx c$. Therefore, the Δ_{CEP} between the drive laser and the mid-IR pulse is fixed at the generation time. To illustrate this point, the dependence of the CEP_{MIR} at $t = 3600T_0$ on the CEP_0 is shown in Figure 4. One can see that the phase difference between CEP_0 and CEP_{MIR} is fixed for the fixed plasma density and length, and there is a nearly linear relationship of the phase difference Δ_{CEP} . The mid-IR pulse peak electric field changes with the variation of the initial CEP_0 , and the direction of peak electric field changes periodically, that is, a linear change from $-\pi$ to 0 with CEP_0 changing from 0 to π , as shown in Figure 4(a). The inset of Figure 4(a) provides the temporal variation of the mid-IR electric field with different CEP_0 (0, $\pi/2$ and π). One can be seen from Figure 4(b) that the CEP_{MIR} is locked on the CEP_0 , and the difference of CEP_{MIR} and CEP_0 is about 0.6π at $t = 3600T_0$, which is in excellent agreement with the theoretical calculation $\Delta_{CEP} \approx 0.6\pi$.

4. Discussion

The process and efficiency of mid-IR pulse generation with the chirp parameter of $b = -0.07$ have been expatiated in the above section. It is significant that the NCLP can effectively enhance the energy conversion efficiency of mid-IR pulses when the NCLP is rapidly compressed in the plasma. To investigate the maximum energy conversion efficiency ($Effi_{max}$) with different chirp parameters, we make the NCLP incident into a semi-infinite plasma channel at $x \geq 0$. We show the results of different negative chirp parameters in Table 1, where t_{MIR} is the diagnosing time. The rapid and drastic compression of the NCLP enhances the intensity of the drive pulse and the plasma perturbation, which make the generation time of the mid-IR pulses earlier. It can be seen in Table 1 that the energy conversion efficiency with $b = -0.07$ is increased by about 2.6 times as compared

Table 1. The maximum energy conversion efficiency ($Effi_{max}$) of the generated mid-IR pulse with different chirp parameters.

	t_{MIR}	$Effi_{max}$	Width (μm)
$b = -0.07$	$4125T_0$	5.0%	4.2–20.0
$b = -0.06$	$4300T_0$	4.6%	4.4–20.0
$b = -0.04$	$4725T_0$	2.7%	6.2–26.6
$b = -0.02$	$5500T_0$	2.3%	6.2–26.6
$b = 0$	$6350T_0$	1.9%	6.2–26.6

to the case of the un-chirped pulse. The improvement of energy conversion efficiency can be attributed to the chirp variation with the same initial laser intensity. The NCLP with $b = -0.07$ corresponds to the Fourier limit duration of about 2.9 fs, which approaches the single laser period of the 0.8 μm wavelength. Therefore, $b = -0.07$ or $R \approx 18.9 \text{ nm/fs}$ is the optimum chirp parameter. In contrast, the energy conversion efficiency with $b = 0.07$ is only about 1% with the peak intensity of $6.3 \times 10^{16} \text{ W cm}^{-2}$, as shown in Figure S1 of the supplementary information. In addition, the generation of mid-IR pulses can be influenced by the plasma density and the down ramp length. More information about the robustness can be seen in the supplementary information.

Finally, we carry out a full-scale 3D PIC simulation as well to ensure the reliability of our scheme. The box size is $60 \mu\text{m}$ (x) \times $60 \mu\text{m}$ (y) \times $60 \mu\text{m}$ (z) with grid cells of $1500 \times 240 \times 240$ and four macroparticles per cell. The incident laser with spot size of $20 \mu\text{m}$ is used in the 3D simulation. The plasma channel has a very long length of plateau, and it allows us to find the best position to generate mid-IR pulses. Transverse slice images of the electric field and electron density at $t = 50T_0$, $t = 3000T_0$ and $t = 5000T_0$ are shown in Figures 5(a)–5(c). One can see in Figures 5(a) and 5(b) that the drive laser pulse excites a stable bubble, which will be a container to accommodate the mid-IR pulse.

The mid-IR pulses can be efficiently generated, and the bubble is full of mid-IR pulses, as shown in Figure 5(c). In addition, we can see that the self-injected electrons overlap spatially with the generated mid-IR pulse. Although the energy exchange can occur between the electron beam and the generated mid-IR pulse, the electron beam is not able to seriously affect the beam quality of the mid-IR pulse due to the short interaction time in our scheme. The spectra at different times are shown in Figure 5(d), where one can see that the maximum central wavelength of the mid-IR pulse is $6 \mu\text{m}$ at $t = 5000T_0$. The average refractive index gradient is estimated to be $-9.3 \times 10^{-3} \mu\text{m}^{-1}$ at the conversion stage from $t = 4000T_0$ to $t = 5000T_0$ in the 3D PIC simulation. According to Equation (5), the average refractive index gradient of $-9.3 \times 10^{-3} \mu\text{m}^{-1}$ will generate the mid-IR pulse wavelength of $6.7 \mu\text{m}$ in a $800 \mu\text{m}$ convertor. The inset of Figure 5(d) shows the temporal profile of the on-axis mid-IR electric field with the FWHM duration of 80 fs. The simulation result shows that one can obtain a mid-IR pulse with the central wavelength of $6 \mu\text{m}$ and the normalized peak intensity of $a_{\text{MIR}} \approx 3.5$ at $t = 5000T_0$. Further, the maximum energy conversion efficiency can reach 6.3% with the spectral width of $4.3\text{--}20 \mu\text{m}$ at $t = 5300T_0$. More 3D simulation and comparison details for the un-chirped case can be found in the supplementary information.

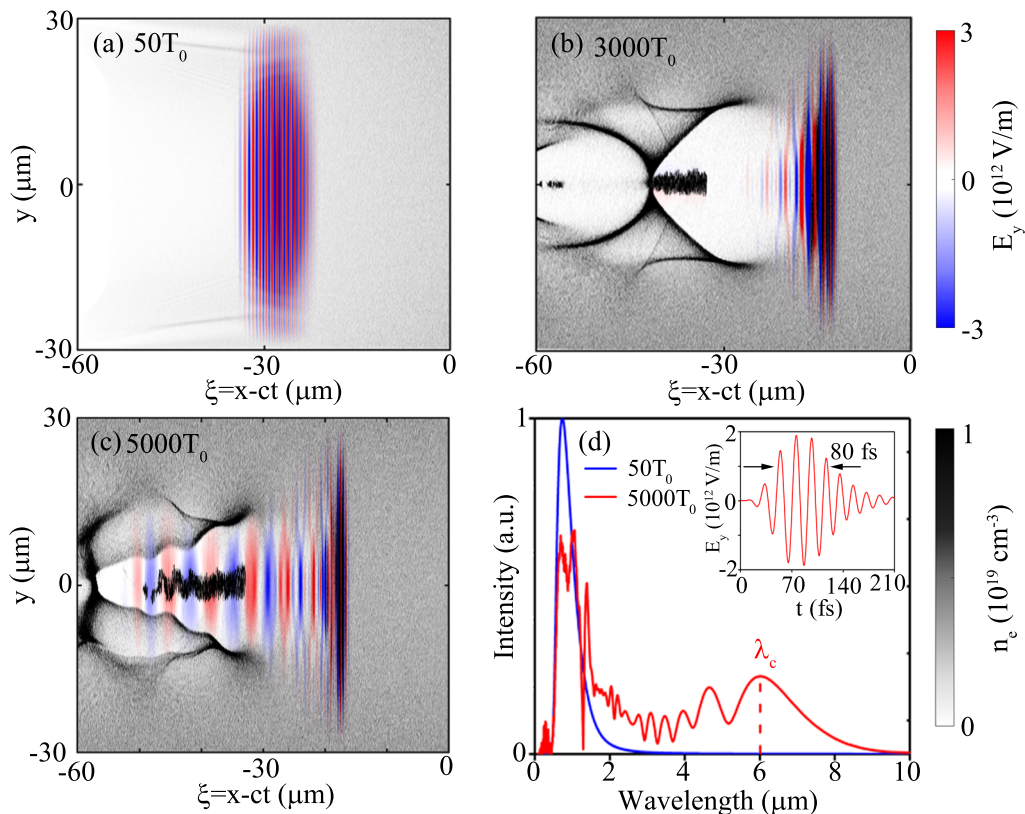


Figure 5. 3D simulation of mid-IR generation with the NCLP. (a)–(c) The distributions of the plasma density (n_e) and the transverse electric field (E_y) at different times obtained from 3D PIC simulation. (d) Spectral distribution of the on-axis laser electric field at $t = 50T_0$ (blue) and $5000T_0$ (red). The inset is the temporal profile of the mid-IR electric field at $t = 5000T_0$.

5. Conclusion

In conclusion, we have proposed and numerically demonstrated a scheme to effectively improve the generation efficiency of high-intensity, few-cycle and long carrier wavelength mid-IR pulses by controlling the chirp parameters of the NCLP. Compared with the case of the un-chirped pulse, due to the difference of phase velocity and group velocity of different frequency components of the NCLP, the plasma etching and the special refractive index can make the pulse rapidly compress longitudinally, and this compression can effectively enhance the pulse intensity and plasma density perturbation. As a result, the mid-IR pulses can be produced faster and the energy conversion efficiency becomes higher. The 2D PIC simulation results show that a relativistic few-cycle mid-IR pulse with a center wavelength of $7.9 \mu\text{m}$ can be generated at an interaction time of $3600T_0$ with the chirped parameter of $b = -0.07$. Meanwhile, the negatively chirped pulse can significantly improve the energy conversion efficiency of mid-IR pulses. The maximum energy conversion efficiency is enhanced to about 5.0% in the case of $b = -0.07$ at an interaction time of $4125T_0$. The 3D PIC simulation results also verify that our scheme can generate a relativistic mid-IR pulse with a higher energy conversion efficiency. The CEP of the generated mid-IR is also phase-locked with the central phase of the initial NCLP. Such efficient mid-IR sources may find many potential applications in high-field physics and ultrafast science, for example, THz emission and charged particle acceleration.

Acknowledgements

We acknowledge the Tianhe supercomputer team for computing resources. This work was supported by the National Key Research and Development Program of China (No. 2018YFA0404802), the National Natural Science Foundation of China (Nos. 12005297, 11875319, 12135009, and 12275356), the Science and Technology Innovation Program of Hunan Province (No. 2020RC4020), the Research Project of NUDT (No. ZK21-12) and the Hunan Provincial Research and Innovation Foundation for Graduate Students (Nos. CX20200002, CX20200038, and CX20210062).

Supplementary Materials

To view supplementary material for this article, please visit <http://doi.org/10.1017/hpl.2023.51>.

References

1. D. Strickland and G. Mourou, *Opt. Commun.* **55**, 447 (1985).
2. G.-P. An, Y.-L. Chi, Y.-L. Dang, G.-Y. Fu, B. Guo, Y.-S. Huang, C.-Y. He, X.-C. Kong, X.-F. Lan, J.-C. Li, F.-L. Liu, J.-S. Shi, X.-J. Sun, Y. Wang, J.-L. Wang, L. Wang, Y.-Y. Wei, G. Wu, G.-L. Xu, X.-F. Xi, G.-J. Yang, C.-L. Zhang, Z. Zhang, Z.-P. Zheng, X.-D. Zhang, and S.-P. Zhang, *Matter Radiat. Extrem.* **3**, 219 (2018).
3. Y.-J. Gu, M. Jirka, O. Klimo, and S. Weber, *Matter Radiat. Extrem.* **4**, 064403 (2019).
4. K. Xue, Z.-K. Dou, F. Wan, T.-P. Yu, W.-M. Wang, J.-R. Ren, Q. Zhao, Y.-T. Zhao, Z.-F. Xu, and J.-X. Li, *Matter Radiat. Extrem.* **5**, 054402 (2020).
5. Y. Lu, G.-B. Zhang, J. Zhao, Y.-T. Hu, H. Zhang, D.-A. Li, Q.-N. Li, Y. Cao, Y.-B. Wu, Y. Yin, F.-Q. Shao, and T.-P. Yu, *Opt. Express* **29**, 8926 (2021).
6. Y.-T. Hu, J. Zhao, H. Zhang, Y. Lu, W.-Q. Wang, L.-X. Hu, F.-Q. Shao, and T.-P. Yu, *Appl. Phys. Lett.* **118**, 054101 (2021).
7. C. Calabrese, A. M. Stingel, L. Shen, and P. B. Petersen, *Opt. Lett.* **37**, 2265 (2012).
8. C. I. Blaga, J. Xu, A. D. DiChiara, E. Sistrunk, K. Zhang, P. Agostini, T. A. Miller, L. F. DiMauro, and C. D. Lin, *Nature* **483**, 194 (2012).
9. B. Wolter, M. G. Pullen, M. Baudisch, M. Sclafani, M. Hemmer, A. Senftleben, C. D. Schröter, J. Ullrich, R. Moshhammer, and J. Biegert, *Phys. Rev. X* **5**, 021034 (2015).
10. W.-M. Wang, S. Kawata, Z.-M. Sheng, Y.-T. Li, L.-M. Chen, L.-J. Qian, and J. Zhang, *Opt. Lett.* **36**, 2608 (2011).
11. T. Popmintchev, M.-C. Chen, D. Popmintchev, P. Arpin, S. Brown, S. Ališauskas, G. Andriukaitis, T. Balčiunas, O. D. Mücke, A. Pugzlys, A. Baltuška, B. Shim, S. E. Schrauth, A. Gaeta, C. Hernández-García, L. Plaja, A. Becker, A. Jaron-Becker, M. M. Murnane, and H. C. Kapteyn, *Science* **336**, 1287 (2012).
12. J. Weisshaupt, V. Juvé, M. Holtz, S. Ku, M. Woerner, T. Elsaesser, S. Ališauskas, A. Pugzlys, and A. Baltuška, *Nat. Photonics* **8**, 927 (2014).
13. I. V. Pogorelsky, M. N. Polyanskiy, and W. D. Kimura, *Phys. Rev. Accel. Beams* **19**, 091001 (2016).
14. D. Woodbury, L. Feder, V. Shumakova, C. Gollner, R. Schwartz, B. Miao, F. Salehi, A. Korolov, A. Pugzlys, A. Baltuška, and H. M. Milchberg, *Opt. Lett.* **43**, 1131 (2018).
15. G.-B. Zhang, N. A. M. Hafz, Y.-Y. Ma, L.-J. Qian, F.-Q. Shao, and Z.-M. Sheng, *Chin. Phys. Lett.* **33**, 095202 (2016).
16. B.-H. Chen, E. Wittmann, Y. Morimoto, P. Baum, and E. Riedle, *Opt. Express* **27**, 21306 (2019).
17. U. Elu, M. Baudisch, H. Pires, F. Tani, M. H. Frosz, F. Köttig, A. Ermolov, P. St. J. Russell, and J. Biegert, *Optica* **4**, 1024 (2017).
18. I. Pupeza, D. Sánchez, J. Zhang, N. Lilienfein, M. Seidel, N. Karpowicz, T. Paasch-Colberg, I. Znakovskaya, M. Pescher, W. Schweinberger, V. Pervak, E. Fill, O. Pronin, Z. Wei, F. Krausz, A. Apolonski, and J. Biegert, *Nat. Photonics* **9**, 721 (2015).
19. P. Krogen, H. Suchowski, H. Liang, N. Flemens, K.-H. Hong, F. X. Kärtner, and J. Moses, *Nat. Photonics* **11**, 222 (2017).
20. J. J. Pigeon, S. Y. Tochitsky, E. C. Welch, and C. Joshi, *Opt. Lett.* **41**, 3924 (2016).
21. F. Junginger, A. Sell, O. Schubert, B. Mayer, D. Brida, M. Marangoni, G. Cerullo, A. Leitenstorfer, and R. Huber, *Opt. Lett.* **35**, 2645 (2010).
22. J. J. Pigeon, S. Y. Tochitsky, C. Gong, and C. Joshi, *Opt. Lett.* **39**, 3246 (2014).
23. D. Haberberger, S. Tochitsky, and C. Joshi, *Opt. Express* **18**, 17865 (2010).
24. M. N. Polyanskiy, I. V. Pogorelsky, and V. Yakimenko, *Opt. Express* **19**, 7717 (2011).
25. L.-L. Yu, Y. Zhao, L.-J. Qian, M. Chen, S.-M. Weng, Z.-M. Sheng, D. A. Jaroszynski, W. B. Mori, and J. Zhang, *Nat. Commun.* **7**, 11893 (2016).
26. J. F. Qu, P. Liu, X. Y. Liu, R. J. Gray, P. McKenna, X. F. Li, S. Kawata, and Q. Kong, *New J. Phys.* **22**, 093007 (2020).

27. A. V. Mitrofanov, A. A. Voronin, D. A. Sidorov-Biryukov, S. I. Mityukovsky, A. B. Fedotov, E. E. Serebryannikov, D. V. Meshchankin, V. Shumakova, S. Ališauskas, A. Pugžlys, V. Y. Panchenko, A. Baltuška, and A. M. Zheltikov, *Optica* **3**, 299 (2016).
28. C.-H. Pai, Y.-Y. Chang, L.-C. Ha, Z.-H. Xie, M.-W. Lin, J.-M. Lin, Y.-M. Chen, G. Tsaur, H.-H. Chu, S.-H. Chen, J.-Y. Lin, J. Wang, and S.-Y. Chen, *Phys. Rev. A* **82**, 063804 (2010).
29. Z. Nie, C.-H. Pai, J. Hua, C. Zhang, Y. Wu, Y. Wan, F. Li, J. Zhang, Z. Cheng, Q. Su, S. Liu, Y. Ma, X. Ning, Y. He, W. Lu, H.-H. Chu, J. Wang, W. B. Mori, and C. Joshi, *Nat. Photonics* **12**, 489 (2018).
30. Z. Nie, C.-H. Pai, J. Zhang, X. Ning, J. Hua, Y. He, Y. Wu, Q. Su, S. Liu, Y. Ma, Z. Cheng, W. Lu, H.-H. Chu, J. Wang, C. Zhang, W. B. Mori, and C. Joshi, *Nat. Commun.* **11**, 2787 (2020).
31. X.-L. Zhu, S.-M. Weng, M. Chen, Z.-M. Sheng, and J. Zhang, *Light. Sci. Appl.* **9**, 46 (2020).
32. Z. Nie, Y. Wu, C. Zhang, W. B. Mori, C. Joshi, W. Lu, C.-H. Pai, J. Hua, and J. Wang, *Phys. Plasmas* **28**, 023106 (2021).
33. X.-L. Zhu, M. Chen, S.-M. Weng, P. McKenna, Z.-M. Sheng, and J. Zhang, *Phys. Rev. Appl.* **12**, 054024 (2019).
34. X.-L. Zhu, W.-Y. Liu, S.-M. Weng, M. Chen, Z.-M. Sheng, and J. Zhang, *Matter Radiat. Extrem.* **7**, 014403 (2022).
35. S. C. Wilks, J. M. Dawson, W. B. Mori, T. Katsouleas, and M. E. Jones, *Phys. Rev. Lett.* **62**, 2600 (1989).
36. E. Esarey, A. Ting, and P. Sprangle, *Phys. Rev. A* **42**, 3526 (1990).
37. W. B. Mori, *IEEE J. Quantum Electron.* **33**, 1942 (1997).
38. W. Zhu, J. P. Palastro, and T. M. Antonsen, *Phys. Plasmas* **20**, 073103 (2013).
39. V. B. Pathak, J. Vieira, R. A. Fonseca, and L. O. Silva, *New J. Phys.* **14**, 023057 (2012).
40. X. Zhang, B. Shen, L. Ji, W. Wang, J. Xu, Y. Yu, L. Yi, X. Wang, N. A. M. Hafz, and V. Kulagin, *Phys. Plasmas* **19**, 053103 (2012).
41. S. Afhami and E. Esлами, *AIP Adv.* **4**, 087142 (2014).
42. M. Rezaei-Pandari, A. R. Niknam, R. Massudi, F. Jahangiri, H. Hassaninejad, and S. M. Khorashadizadeh, *Phys. Plasmas* **24**, 023112 (2017).
43. W.-M. Wang, Z.-M. Sheng, H.-C. Wu, M. Chen, C. Li, J. Zhang, and K. Mima, *Opt. Express* **16**, 16999 (2008).
44. A. Mehta, J. Rajput, K. Kang, and N. Kant, *Laser Phys.* **30**, 045402 (2020).
45. M. C. Gurjar, K. Gopal, D. N. Gupta, V. V. Kulagin, and H. Suk, *IEEE Trans. Plasma Sci.* **48**, 3727 (2020).
46. J.-H. Kim and C. H. Nam, *Phys. Rev. A* **65**, 033801 (2002).
47. E. Neyra, F. Videla, J. A. Pérez-Hernández, M. F. Ciappina, L. Roso, and G. A. Torchia, *Laser Phys. Lett.* **13**, 115303 (2016).
48. P. Sprangle, E. Esarey, and A. Ting, *Phys. Rev. Lett.* **64**, 2011 (1990).
49. P. Sprangle, E. Esarey, and A. Ting, *Phys. Rev. A* **41**, 4463 (1990).
50. L. Ghasemi, S. Afhami, and E. Esلامي, *Phys. Plasmas* **22**, 082123 (2015).
51. A. G. Khachatryan, F. A. van Goor, and K.-J. Boller, *Phys. Rev. E* **70**, 067601 (2004).
52. T. D. Arber, K. Bennett, C. S. Brady, A. Lawrence-Douglas, M. G. Ramsay, N. J. Sircombe, P. Gillies, R. G. Evans, H. Schmitz, A. R. Bell, and C. P. Ridgers, *Plasma Phys. Control. Fusion* **57**, 113001 (2015).
53. A. K. Brodzik, *IEEE Signal Proc. Lett.* **13**, 541 (2006).
54. Y. Su, S. Fang, Y. Gao, K. Zhao, G. Chang, and Z. Wei, *Appl. Phys. Lett.* **118**, 261102 (2021).
55. E. Esarey, C. B. Schroeder, and W. P. Leemans, *Rev. Mod. Phys.* **81**, 1229 (2009).
56. C. G. R. Geddes, C. Toth, J. van Tilborg, E. Esarey, C. B. Schroeder, D. Bruhwiler, C. Nieter, J. Cary, and W. P. Leemans, *Nature* **431**, 538 (2004).
57. Y. Mizuta, T. Hosokai, S. Masuda, A. Zhidkov, K. Makito, N. Nakanii, S. Kajino, A. Nishida, M. Kando, M. Mori, H. Kotaki, Y. Hayashi, S. V. Bulanov, and R. Kodama, *Phys. Rev. Spec. Top. Accel. Beams* **15**, 121301 (2012).
58. J. Huijts, I. A. Andriyash, L. Rovige, A. Vernier, and J. Faure, *Phys. Plasmas* **28**, 043101 (2021).